

Rational Design of a Novel Catalyst Cu-SAPO-42 for NH₃-SCR Reaction

Nana Yan, Chao Ma, Yi Cao, Xiaona Liu, Lei Cao, Peng Guo,* Peng Tian,* and Zhongmin Liu*

Cu-exchanged LTA-type aluminosilicate catalyst has been considered as an efficient catalyst for the selective catalytic reduction of NO_x with ammonia (NH₃-SCR). However, expensive organic structure-directing agents (OSDAs) and the corrosive fluoride medium are inevitably used to synthesize LTA-type molecular sieve (high-silica LTA-type aluminosilicate and its analogue LTA-type silicoaluminophosphate SAPO-42). Herein, a series of cheap and commercialized OSDAs, which are successfully applied for the targeted synthesis of SAPO-42 in the fluoride-free system, are identified by a novel RSS (refine, summarize, and search) approach. Furthermore, Cu-SAPO-42 catalysts are utilized for NH₃-SCR. Among these catalysts, Cu-SAPO-42 prepared with 2-(butylamino)ethanol (BAEA) as OSDA demonstrates the excellent activity even after hydrothermal aging at 800 °C for 16 h, which shows much better hydrothermal stability than the commercialized Cu-SAPO-34 catalyst with comparable Si and Cu contents. Electron paramagnetic resonance (EPR) spectroscopy and Rietveld refinement are performed to identify the locations of active Cu²⁺ ions. It turns out that the active Cu²⁺ ions are distributed near the center of single 6-rings of the *lta* cage.

vehicles have become stricter. At present, selective catalytic reduction of NO_x with ammonia (NH₃-SCR) has been regarded as the most efficient technology to facilitate the NO_x reduction in oxygen-rich exhaust released from diesel engines.^[1–4] Metal-exchanged conventional aluminosilicate zeolites or silicoaluminophosphates (SAPO) molecular sieves (MSs) have been extensively investigated for catalyzing this reaction. Zeolites or SAPO MSs are a class of crystalline microporous materials with well-defined cavities or channels of molecular size. TO₄ tetrahedra (T = Al, Si, P, etc.) are considered as basic building units (BBUs). Until now, distinct 252 three-dimensional (3D) zeolitic frameworks constructed by BBUs have been approved by IZA-structure committee.^[5] They can be categorized into small pore (delimited by 8 T), medium pore (10 T), large pore (12 T), and extra-large pore (>12 T) MSs. Thereinto, small pore MSs, especially

aluminosilicate SSZ-13 and SAPO-34 with the identical CHA framework, have been regarded as the efficient catalysts for the NH₃-SCR reaction due to their high NO_x conversion and N₂ selectivity.^[3] Although Cu-SSZ-13 catalyst has been commercialized, its thermal durability after the high-temperature (HT) hydrothermal aging, arising from the regeneration process of diesel particulate filter (DPF), can be further improved. Moreover, Cu-SAPO-34 catalyst has some disputes on the low-temperature (LT) hydrothermal stability. Therefore, it stimulates the interest of researchers to explore other novel zeolite frameworks with small pore openings. Recently, Hong et al. have reported a Cu exchanged LTA-type high-silica (3D 8 × 8 × 8-ring channel system) zeolite which has the better activity and durability than Cu-SSZ-13 after HT hydrothermal aging.^[6,7] However, the expensive organic structure-directing agents (OSDAs) and the presence of the toxic fluoride used in its recipe might inhibit its further utilization as an NH₃-SCR catalyst. It is of interest to note that SAPO-42 with the LTA topology might be a potential catalyst for the NH₃-SCR reaction.

The initial synthesis of SAPO-42 templated by TMA⁺ and Na⁺ was reported in 1984.^[8,9] Strictly speaking, it is not an exact SAPO since only a few portions of phosphor are incorporated into the framework. After that, several works reported the synthesis of SAPO-42 by using complex OSDAs in the fluoride system or the ionothermal synthesis.^[10–13] For example, Corma's

1. Introduction

Environmental issues have received much attention, and the pursuit of clean air is becoming stronger. Therefore, the emission standards of nitrogen oxides (NO_x) exhausted from diesel

N. Yan, C. Ma, Dr. Y. Cao, X. Liu, Dr. L. Cao, Dr. P. Guo, Prof. P. Tian, Prof. Z. Liu
National Engineering Laboratory for Methanol to Olefins
Dalian Institute of Chemical Physics
Chinese Academy of Sciences
Dalian 116023, P.R. China
E-mail: pguo@dicp.ac.cn; tianpeng@dicp.ac.cn; zml@dicp.ac.cn

N. Yan, C. Ma, X. Liu
University of Chinese Academy of Sciences
Beijing 100049, P.R. China

C. Ma
Zhang Dayu School of Chemistry
Dalian University of Technology
Dalian 116024, P.R. China

Dr. Y. Cao
School of Material Science and Chemical Engineering
Ningbo University
Ningbo 315211, P.R. China

 The ORCID identification number(s) for the author(s) of this article can be found under <https://doi.org/10.1002/sml.202000902>.

DOI: 10.1002/sml.202000902

group employed self-assembled aromatic molecules as OSDAs for synthesizing SAPO-42 in 2015.^[11] Unfortunately, the expensive complex OSDA and the toxic fluoride medium were still used. Very recently, our group has reported the targeted synthesis of DNL-6 (a small-pore SAPO MS with **RHO** topology) using a newly developed **RSS** approach, which is mainly based on understanding the host (SAPO framework)–guest (OSDA) interaction unravelled by Rietveld refinement.^[14] By using the **RSS** approach, we have not only extended the synthesis of DNL-6 with a series of OSDAs predicted, but also obtained SAPO-42 using a “symmetric” commercialized dipropylamine (DPA) as the OSDA in the fluoride-free system.

Herein, in this work, we use the **RSS** approach for exploring the synthesis of SAPO-42 from “symmetric” secondary amines to a series of “asymmetric” ones. Moreover, Cu-SAPO-42 catalysts synthesized by different OSDAs are employed for the NH₃-SCR reaction. Among these catalysts, Cu-SAPO-42 templated by 2-(butylamino)ethanol (BAEA) remains the excellent NO conversion at the temperature above 250 °C even after hydrothermal aging at 800 °C for 16 h.

2. Results and Discussion

2.1. Targeted Synthesis of SAPO-42 Using RSS Approach

The **RSS** method includes three steps: 1) Refine known samples against experimental diffraction data and then identify the locations of OSDA and host–guest interactions, 2) Summarize the structural features of OSDA, and 3) Search for suitable OSDA candidates. In our previous systematic work regarding the synthesis of DNL-6s templated by a series of secondary amines, Rietveld refinement of known DNL-6-DEA and DNL-6-DMEDA was first conducted. It turns out that the protonated OSDAs form the classical hydrogen bonding interactions with O atoms in the 8-rings, which connect *lta* cage and *d8r*. Meanwhile, the shorter alkyl groups of OSDAs stretch into *d8r*, while the larger one can stabilize the *lta* cage (Steps 1 and 2 of **RSS** in DNL-6). According to these structural features, 14 OSDA candidates were selected (Step 3 of **RSS** in DNL-6), and pure phase DNL-6s templated by nine of them as OSDA were obtained.^[14] In DNL-6s, the alkyl group stabilizing *lta* cages can be from linear chains (such as ethyl, propyl, and butyl) to branched chains, even cyclic alkyl group. Furthermore, in the case of SAPO-42-DPA (**LTA**), the N atom of “symmetric” DPA stuck in the 8-rings forms the hydrogen bond with O atoms in the single 8-rings, and the propyl groups support the two *lta* cages on both sides (Steps 1 and 2 of **RSS** in SAPO-42). It has been demonstrated that amines with symmetric structure have the ability to direct SAPO-42. Inspired by our such investigations, it is reasonable that “asymmetric” amines with appropriate groups, which can stabilize *lta* cages, will be promising OSDAs for extending the synthesis of SAPO-42. Therefore, a group of commercialized “asymmetric” secondary amines (including alcohol amine) as listed in **Figure 1a** are selected as OSDAs to synthesize SAPO-42 (Step 3 of **RSS**). It is worth pointing that ethyl is not only suitable to support *d8rs*, but also can stabilize *lta* cage, which has been confirmed in the synthesis of DNL-6 templated by diethylamine and methylethylamine. To verify the directing ability of selected amines, initial

synthesis trials were performed using the recipe modified from the gel composition of SAPO-42-DPA. The synthesis details are listed in Table S1 (Supporting Information). SAPO-42 appeared as the well-crystallized pure phase (IPAEA, EPA, and EBA) or the main phase along with some impurities or amorphous (BAEA, BnIPA, and EBnA) as shown in PXRD (powder X-ray diffraction) results (**Figure 1b**), which demonstrates the availabilities of new “asymmetric” OSDAs for SAPO-42.

For purifying SAPO-42s templated BAEA, BnIPA, and EBnA, the synthesis conditions were further optimized through adjusting gel compositions, changing raw materials, the amount of seed addition, and crystallization time. Finally, four pure SAPO-42 samples as listed in Table S2 (Supporting Information) were obtained by using IPAEA, EPA, EBA, and BAEA as OSDAs (XRD results in **Figure S1** (Supporting Information) and SEM images in **Figure S3**, Supporting Information), denoted as SAPO-42-OSDA. A little SAPO-5 accompanied by SAPO-42-BnIPA and SAPO-42-EBnA (**Table S3** and **Figure S2**, Supporting Information). ¹³C MAS NMR results confirm that OSDAs occluded within *lta* cage are intact (**Figure S4**, Supporting Information). Combined with the results of TGA and XRF, the unit cell composition of SAPO-42 samples could be deduced as demonstrated in **Table S2** (Supporting Information). The content of Si is slightly different, ranging from 32.8 to 35.6 Si per unit cell when various OSDAs are used. Moreover, ²⁹Si MAS NMR of SAPO-42-IPAEA with higher Si contents and SAPO-42-BAEA with lower Si contents have been performed to explore the local atomic environment of Si, as illustrated in **Figure 1c**. The strong peak at –92 ppm suggests the most presence of Si(OAl)₄ species in the framework and the other signals at –96, –100, and –110 ppm indicate the presence of Si island in both samples.

2.2. Rietveld Refinements of SAPO-42s Synthesized by Asymmetric OSDAs

The purely well-crystallized SAPO-42 samples enable us to collect the high-quality PXRD data for further structural investigation through Rietveld refinement. In our previous work, we have utilized Rietveld refinement against the high-resolution PXRD data combined with the simulated annealing algorithms to investigate the Brønsted acids confined in the **FER**-type zeolite and facilitate the targeted synthesis of SAPO MSs.^[14–16] In this work, precise locations of OSDAs and the host–guest interaction between OSDA and framework are explored by this combined methodology as well. The idealized pure-silica **LTA** framework with the space group of *Pm3m* (No. 221) has only one T atom and three O atoms in the asymmetric unit. However, the type material, aluminosilicate zeolite A, possesses the alternating distribution of Al and Si. The cubic unit cell parameter is doubled compared with the one of idealized pure-silica **LTA** framework, while its space group is changed to *Fm-3c* (No. 226) accordingly. This scenario resembles the alternating distribution of Al and P in SAPO MSs. Therefore, the space group and initial atomic coordinates of SAPO-42 adopted from crystallographic information of zeolite A deposited in the database.^[5] And then its structure was optimized through geometrical refinement against the angle and distance restraints based on the SAPO chemical compositions (details in Supporting Information). Take SAPO-42-BAEA as an

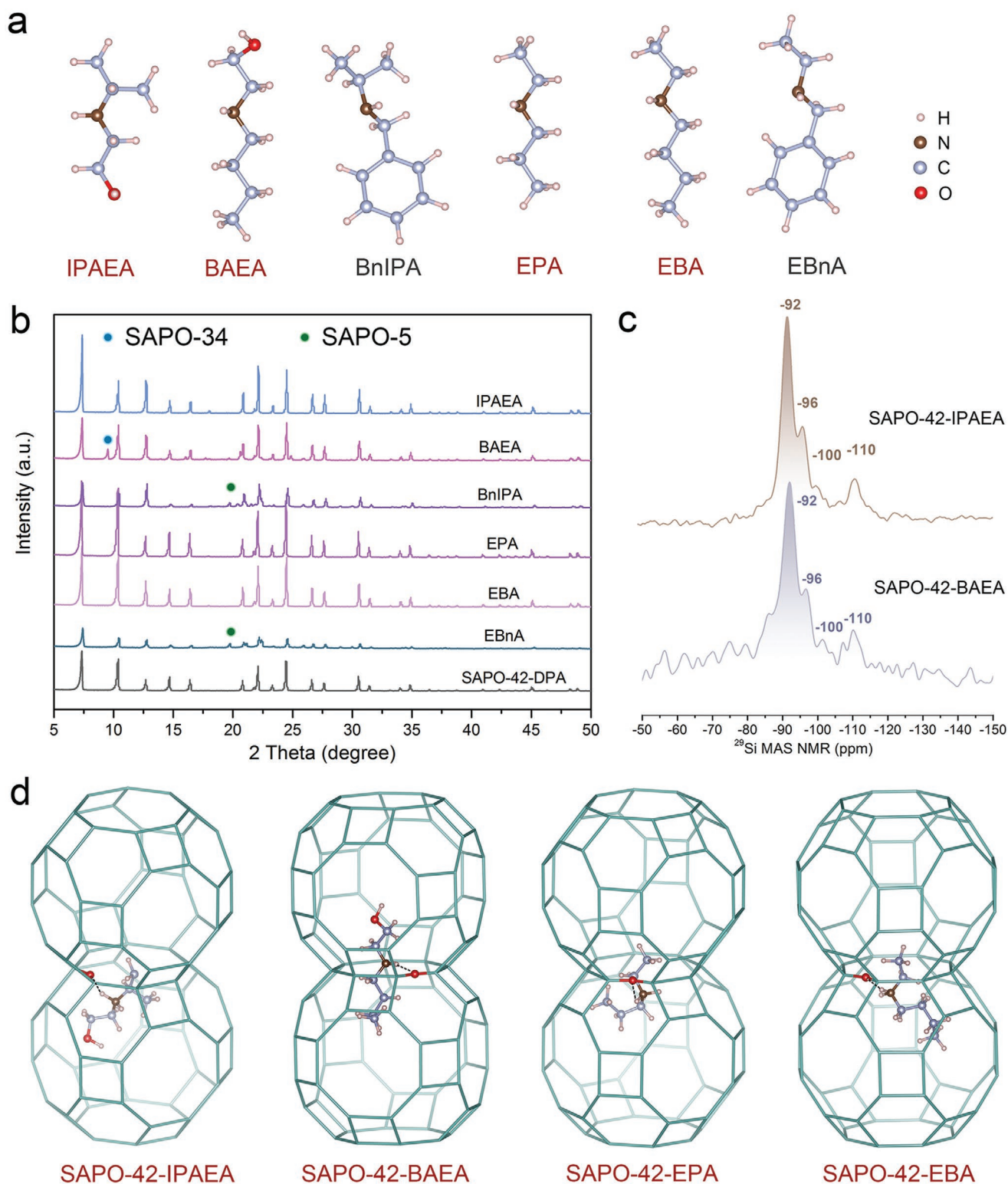


Figure 1. a) A group of commercialized asymmetric secondary amines (including alcohol amine). b) Powder X-ray diffraction (PXRD) results of the initial tentative synthesis with six types of amines listed in (a). c) ^{29}Si MAS NMR spectra of SAPO-42-IPAEA and SAPO-42-BAEA. d) The locations of organic structure-directing agents (OSDAs) and host-guest interactions in the SAPO-42-IPAEA, SAPO-42-BAEA, SAPO-42-EPA, and SAPO-42-EBA. For clarity, the O atoms were omitted except for the one which makes the hydrogen bonding interaction with the N atom of OSDA. The highly disordered water molecules have also been omitted for clarity.

example for the further explanation. The difference electron density map calculated by the experimental PXRD data and simulated one of SAPO-42 framework (without OSDAs) was shown in Figure S5 (Supporting Information), which indicates the positions of OSDAs. Then, the simulated annealing is applied to determine the initial locations of OSDAs. The final refinement converged to $R_p = 0.017$ and $R_{wp} = 0.026$ (Figure 1d, Figure S7 and Table S4, Supporting Information). As shown in Figure 1d, locations of OSDAs (IPAEA, EPA, EBA, and BAEA) and host-guest interactions in the four SAPO-42 samples revealed by this combined methodology are similar. The N atoms of OSDAs make hydrogen bonding interactions with the O atoms in single 8-rings (Figure 1d and Table S4, Supporting Information), which connects neighbouring *lta* cages. And two different groups distributed on both sides of N atom in OSDAs stabilize adjacent *lta* cages. Since the steric hindrance on both sides of “asymmetric” OSDAs is different, the N atoms deviate from the “mirror plane” single 8-rings to one of *lta* cages, making the hydrogen bonds longer. These structural features are consistent with our previous observations in the DNL-6s and SAPO-42-DPA.

2.3. NH₃-SCR Catalytic Performance of Cu-SAPO-42

Considering the promising performance of Cu exchanged small-pore MSs with larger cages in the NH₃-SCR reaction, Cu-SAPO-42s synthesized by different OSDAs are investigated as catalysts for this process. First, the five SAPO-42 samples including SAPO-42-DPA, SAPO-42-IPAEA, SAPO-42-EPA, SAPO-42-EBA, and SAPO-42-BAEA were prepared to exchange with Cu by the direct ion exchange method, details in Supporting Information. For the better comparison, the Cu exchanged level was controlled to 100% approximately (Cu/Brønsted acidic sites = 0.50). The final Cu loadings were measured by XRF before the calcination as listed in Table S5 (Supporting Information), and the corresponding calcined samples were denoted as Cu-SAPO-42-OSDA-CuO wt%. In this case, the amounts of CuO in all the catalysts will be approximately 6 wt%.

The NH₃-SCR activities of the fresh catalysts prepared with different OSDAs are illustrated in Figure 2a. Cu-SAPO-42-EBA-6.5% and Cu-SAPO-42-EPA-6.4% have undesirable activities in the entire temperature ranges. The activities of the

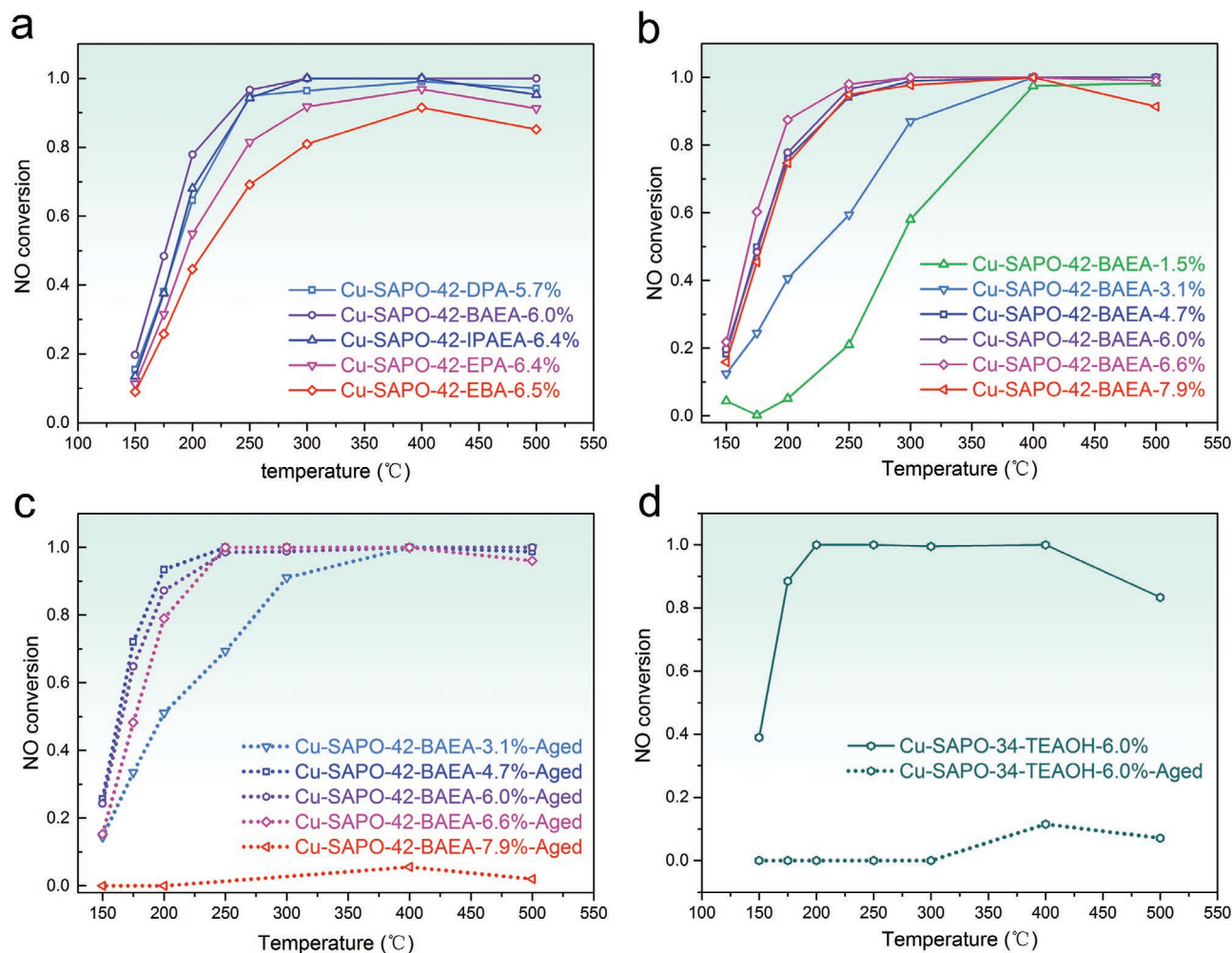


Figure 2. NH₃-SCR performance of Cu-SAPO-42 and Cu-SAPO-34. a) Fresh activities of Cu-SAPO-42 templated by different organic structure-directing agents (OSDAs). b,c) The activities of fresh Cu-SAPO-42-BAEA with different Cu contents and the activities of corresponding catalysts after hydrothermal aging at 800 °C. d) NH₃-SCR performance of Cu-SPA0-34-TEAOH-6.0% before and after hydrothermal aging at 800 °C. The feed contains 500 ppm NO, 500 ppm NH₃, 6.1% O₂, and 6.4% H₂O balanced with N₂ at 300 000 h⁻¹ gas hourly space velocity (GHSV).

other three samples at temperature below 250 °C increase as follows: Cu-SAPO-42-DPA-5.7% < Cu-SAPO-42-IPAEA-6.4% < Cu-SAPO-42-BAEA-6.0%, and they all perform high NO_x conversion at the temperature above 250 °C. Furthermore, all Cu-SAPO-42 catalysts present excellent N₂ selectivity and less N₂O products (Figure S12, Supporting Information). It turns out that the reaction activities are highly associated with Cu-SAPO-42 catalysts templated by different OSDAs. Such a phenomenon has been reported in Cu-SAPO-34 catalysts.^[17] Among these catalysts, Cu-SAPO-42-BAEA-6.0% shows the best NH₃-SCR performance.

Therefore, a series of Cu-SAPO-42-BAEA with different Cu contents were prepared, i.e., different Cu/Bronsted acidic sites (Table S5, Supporting Information), and their catalytic activities are displayed in Figure 2b. It is of significance to note that NO_x conversions of Cu-SAPO-42 catalysts increase with the increment of CuO content until it reaches 6.6%, while further increasing the CuO content will result in the decreased activity in the NH₃-SCR reaction. After HT hydrothermal aging in air flow containing 10% vapor at 800 °C for 16 h, except Cu-SAPO-42-BAEA-6.6% and Cu-SAPO-42-BAEA-7.9% with ultra-high CuO contents, the activities of Cu-SAPO-42-BAEA catalysts with the loading of CuO < 6.6% in the LT range increase and their activities in HT range maintain completely (100%; Figure 2c). The improved activities after HT hydrothermal aging might be attributed to the redistribution of active species, which will be discussed in the following paragraph.^[18,19] Although the fresh activity of Cu-SAPO-42-BAEA-6.6% is remarkable, it declines after HT hydrothermal aging, which might be attributed to the degradation of framework crystallinity (Figure S14, Supporting Information). Considering both fresh activities and the ones after HT hydrothermal aging comprehensively, it is notable that Cu-SAPO-42-BAEA-4.7% and Cu-SAPO-42-BAEA-6.0% display better activities than the others. Besides, activity tests with higher GHSV 400000 and 500000 h⁻¹ have been performed over the catalysts of Cu-SAPO-42-BAEA-4.7% and Cu-SAPO-42-BAEA-6.0% (Figure S15, Supporting Information). With the increase of GHSV, the fresh activity of Cu-SAPO-42-BAEA-6.0% is better than Cu-SAPO-42-BAEA-4.7%.

As a controlled experiment, Cu-SAPO-34 with similar Si contents and Cu contents to Cu-SAPO-42-BAEA-6.0% was also prepared as shown in Table S5 (Supporting Information).

Notably, the activity of Cu-SAPO-34-TEAOH-6.0% is better than Cu-SAPO-42-BAEA-6.0% at the temperature below 250 °C, while its activity slightly decreases at the temperature above 400 °C (Figure 2d). Moreover, it entirely loses activity after HT hydrothermal aging process, due to the collapse of structure (Figure S16, Supporting Information).

2.4. Catalysts Characterizations

To further understand the differences in the catalytic properties of SAPO-42-BAEA-6.0% and Cu-SAPO-34-TEAOH-6.0% for NH₃-SCR, characterizations including NH₃-TPD, EPR, and Rietveld refinement have been performed. The acid properties of catalysts are important to the NH₃-SCR activity. As shown in Figure 3a, there is a distinct difference in the intrinsic acid strength between H-SAPO-42-BAEA and H-SAPO-34-TEAOH. The desorption peak at the lower temperature is attributed to weakly adsorbed NH₃, including the contributions of physical absorption NH₃ and NH₃ adsorbed on terminated hydroxyls (P-OH or Al-OH), while the one at higher temperature is related to Bronsted acid sites.^[7,20] Therefore, the Bronsted acid strength of H-SAPO-42-BAEA is more moderate than H-SAPO-34-TEAOH. To identify the desorption NH₃ from Cu exchanged sample, in situ NH₃-TPD DRIFT of Cu-SAPO-42-BAEA-6.0% was performed and detailed in Figures S18 and S19 (Supporting Information).

EPR was employed to probe structural information of isolated Cu²⁺ in dehydrated fresh catalysts. Cu-SAPO-34-TEAOH-6.0% has two types of Cu²⁺ positions (Figure 3b). The much higher intensity signal of $g_{||} = 2.36$, $A_{||} = 137$ G indicates that Cu²⁺ is mainly distributed under the double 6-rings of the framework.^[20,21] Furthermore, there are also two types of Cu²⁺ positions in the Cu-SAPO-42-BAEA-6.0% evidenced by the EPR result (Figure 3b,c). The signal of $g_{||} = 2.36$, $A_{||} = 137$ G can be assigned to Cu²⁺ located in the center of single 6-ring (s6r) (Site I), while the other one of $g_{||} = 2.40$, $A_{||} = 113$ G is related to Cu²⁺ located adjacent to the s6r but displaced into the *lta* cage (Site II).^[6] Thus, the local environment of Cu²⁺ in Cu-SAPO-42 is essentially distinct from Cu-SAPO-34.

In addition, Cu-SAPO-42-BAEA with different Cu loadings and the corresponding HT hydrothermally aged catalysts have

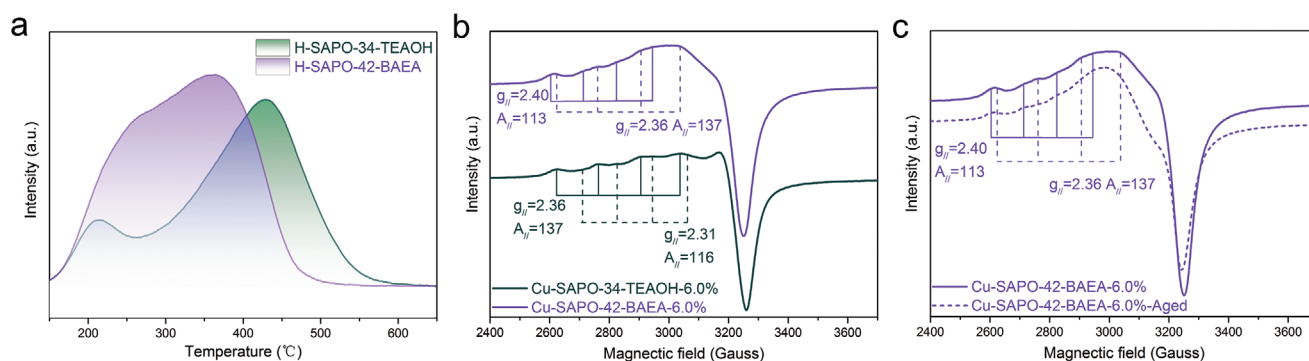


Figure 3. a) NH₃-TPD of H-SAPO-42-BAEA (purple curve) and H-SAPO-34-TEAOH (green curve). b) Electron paramagnetic resonance (EPR) results of Cu-SAPO-42-BAEA-6.0% (purple curve) and Cu-SAPO-34-TEAOH-6.0% (green curve). c) EPR results of Cu-SAPO-42-BAEA-6.0% before and after hydrothermal aging at 800 °C for 16h.

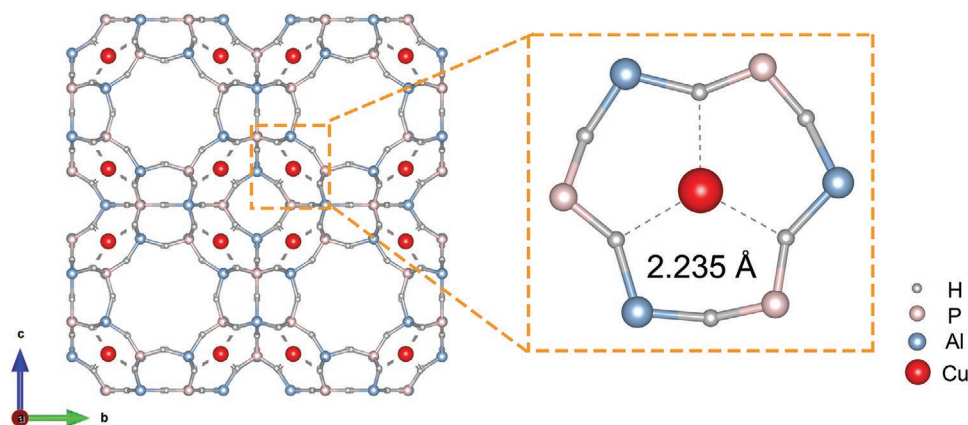


Figure 4. The crystallographic structures of Cu-SAPO-42-BAEA-6.0%-Aged from Rietveld refinement. Cu^{2+} ions locate near the center of $6r$.

been characterized. With the increase of Cu loading in Cu-*SAPO*-42-BAEA, the content of isolated Cu^{2+} increases until the exchange level reaches to ≈ 0.5 (*SAPO*-42-BAEA-6.0%) and then decreases (Figure S21, Supporting Information). Figure 3c shows that Cu-*SAPO*-42-BAEA-6.0% and its corresponding HT hydrothermally aged catalyst Cu-*SAPO*-42-BAEA-6.0%-Aged have similar EPR signals. Moreover, the HT hydrothermal aging process makes Cu species redistributed and the amount of isolated Cu^{2+} in Cu-*SAPO*-42-BAEA-6.0%-Aged increases than the fresh one (Figure S21, Supporting Information). Rietveld refinement was also carried out to determine the precise coordinates of Cu^{2+} in Cu-*SAPO*-42-BAEA-6.0%-Aged, ignoring the effect of disordered CuO particles as shown in TEM (Figure S22, Supporting Information). Since Cu^{2+} ions in the sites I and II are too close to distinguish, an average location of Cu^{2+} near the center of $6r$ can be identified. Its coordinates to three framework oxygen atoms as shown in **Figure 4**, which resembles the location of Cu^{2+} in the fresh aluminosilicate Cu-LTA catalyst.^[6] The further exploration regarding LT hydrothermal stability of Cu-*SAPO*-42 catalyst is still under investigation.

3. Conclusion

In conclusion, copper exchanged *SAPO*-42 samples, which were synthesized with different secondary amines as OSDA in the fluoride-free system through the **RSS** approach, have shown the promising activity in NH_3 -SCR even after hydrothermal aging at 800 °C for 16 h, especially for the Cu-*SAPO*-42-BAEA catalyst. Its comprehensive catalytic performance is much superior to the commercialized Cu-*SAPO*-34 catalyst with comparable Si and Cu contents. Moreover, Rietveld refinement was further used for probing the active Cu^{2+} ions in the Cu-*SAPO*-42-BAEA-6.0%-Aged catalyst. It turned out they are distributed near the center of single 6-rings of the *lta* cage. This new synthetic methodology might open an avenue for the targeted synthesis of specific *SAPO* MSs with tailored catalytic performance in the near future.

[CCDC 1978220–1978224 contains the supplementary crystallographic data for this paper. These data can be obtained free of charge from The Cambridge Crystallographic Data Centre via www.ccdc.cam.ac.uk/data_request/cif.]

Supporting Information

Supporting Information is available from the Wiley Online Library or from the author.

Acknowledgements

N.Y., C.M. contributed equally to this work. Dr. P.G. acknowledges financial support from the National Natural Science Foundation of China (No. 21972136) and the CAS Pioneer Hundred Talents Program (Y706071202). Prof. P.T. acknowledges financial support from the National Natural Science Foundation of China (No. 21676262 and No. 21991091) and Key Research Program of Frontier Sciences, Chinese Academy of Sciences (Grant No. QYZDBSSW-JSC040). Dr. L.C. acknowledges financial support from the National Natural Science Foundation of China (No. 21606221).

Conflict of Interest

The authors declare no conflict of interest.

Keywords

molecular sieves, NH_3 -SCR, porous materials, *SAPO*-LTA, targeted synthesis

Received: February 12, 2020

Revised: June 7, 2020

Published online: July 19, 2020

- [1] C. Paolucci, I. Khurana, A. A. Parekh, S. Li, A. J. Shih, H. Li, J. R. Di Iorio, J. D. Albarracin-Caballero, A. Yezerets, J. T. Miller, W. N. Delgass, F. H. Ribeiro, W. F. Schneider, R. Gounder, *Science* **2017**, 357, 898.
- [2] A. M. Beale, F. Gao, I. Lezcano-Gonzalez, C. H. F. Peden, J. Szanyi, *Chem. Soc. Rev.* **2015**, 44, 7371.
- [3] E. Borfecchia, P. Beato, S. Svelle, U. Olsbye, C. Lamberti, S. Bordiga, *Chem. Soc. Rev.* **2018**, 47, 8097.
- [4] L. Zhang, Q. Wu, X. Meng, U. Müller, M. Feyen, D. Dai, S. Maurer, R. McGuire, A. Moini, A.-N. Parvulescu, W. Zhang, C. Shi, T. Yokoi, X. Pan, X. Bao, H. Gies, B. Marler, D. E. De Vos, U. Kolb, F.-S. Xiao, *React. Chem. Eng.* **2019**, 4, 975.
- [5] Database of Zeolite Structures, <http://www.iza-structure.org/databases/> (accessed: 2017).

- [6] T. Ryu, N. H. Ahn, S. Seo, J. Cho, H. Kim, D. Jo, G. T. Park, P. S. Kim, C. H. Kim, E. L. Bruce, P. A. Wright, I.-S. Nam, S. B. Hong, *Angew. Chem., Int. Ed.* **2017**, *56*, 3256.
- [7] D. Jo, G. T. Park, T. Ryu, S. B. Hong, *Appl. Catal., B* **2019**, *243*, 212.
- [8] B. M. Lok, C. A. Messina, R. L. Patton, R. T. Gajek, T. R. Cannan, E. M. Flanigen, *J. Am. Chem. Soc.* **1984**, *106*, 6092.
- [9] B. M. Lok, C. A. Messina, R. L. Patton, R. T. Gajek, T. R. Cannan, E. M. Flanigen, *U.S. Patent 4,440*, **1984**.
- [10] L. Sierra, C. Deroche, H. Gies, J. L. Guth, *Microporous Mat.* **1994**, *3*, 29.
- [11] R. Martínez-Franco, Á. Cantín, A. Vidal-Moya, M. Moliner, A. Corma, *Chem. Mater.* **2015**, *27*, 2981.
- [12] J. E. Schmidt, S. I. Zones, D. Xie, M. E. Davis, *Microporous Mesoporous Mater.* **2014**, *200*, 132.
- [13] Y. Lin, Y. Wei, L. Zhang, K. Guo, M. Wang, P. Huang, X. Meng, R. Zhang, *Microporous Mesoporous Mater.* **2019**, *288*, 109611.
- [14] N. Yan, L. Wang, X. Liu, P. Wu, T. Sun, S. Xu, J. Han, P. Guo, P. Tian, Z. Liu, *J. Mater. Chem. A* **2018**, *6*, 24186.
- [15] L. Wang, H. Xu, N. Yan, S. Correll, S. Xu, P. Guo, P. Tian, Z. Liu, *CrystEngComm* **2018**, *20*, 699.
- [16] N. Yan, H. Xu, W. Zhang, T. Sun, P. Guo, P. Tian, Z. Liu, *Microporous Mesoporous Mater.* **2018**, *264*, 55.
- [17] J. Woo, K. Leistner, D. Bernin, H. Ahari, M. Shost, M. Zammit, L. Olsson, *Catal. Sci. Technol.* **2018**, *8*, 3090.
- [18] J. Wang, T. Yu, X. Wang, G. Qi, J. Xue, M. Shen, W. Li, *Appl. Catal., B* **2012**, *127*, 137.
- [19] J. Tang, M. Xu, T. Yu, H. Ma, M. Shen, J. Wang, *Chem. Eng. Sci.* **2017**, *168*, 414.
- [20] Y. Cao, D. Fan, L. Sun, M. Yang, L. Cao, T. Sun, S. Xu, P. Tian, Z. Liu, *Chem. Eng. J.* **2019**, *374*, 832.
- [21] Y. Cao, D. Fan, P. Tian, L. Cao, T. Sun, S. Xu, M. Yang, Z. Liu, *Chem. Eng. J.* **2018**, *354*, 85.